On some physical phenomena involved in blade-casing contact

Patricio Almeida, Claude Gibert, Fabrice Thouverez, Jean-Philippe Ousty

On some physical phenomena involved in blade-casing contact

P. Almeida[a]*, C. Gibert [a], F. Thouverez[a], J.-P. Ousty[b]
[(a)] École Centrale de Lyon, Laboratoire de Tribologie et Dynamique des Systèmes
36 avenue Guy de Collongue, 69134 Ecully Cedex, France
[(b)] Turbomeca – Safran Group, 64511 Bordes cedex, France
patricio.almeida@ec-lyon.fr

ABSTRACT: One of the undesirable phenomena in turbomachinery is linked to the contact between rotating and stationary parts, which is more likely to occur when clearance is minimized in order to improve aerodynamic efficiency. These mechanical characteristics favor energy exchanges between the two structures, and this in turn may lead to high dynamic excitations of the impeller and stator or even to unstable vibrations. Lot of numerical studies have been conducted in order to derive a better understanding of the dynamic behavior taking place during blade-to-casing contact. However, the influence of other physical phenomena, such as wear and heating, remain poorly understood. A recent experimental study shows that the dynamic behavior of structures is significantly influenced by both wear and thermal expansion. The focus of this paper therefore is show some effects associated with friction and wear.
The numerical study reported in this paper is based on a simplified finite element model of a rotating bladed disk and a flexible casing. The contact algorithm uses an explicit time marching scheme with the Lagrange multipliers method. Friction and wear are formulated respectively by Coulomb's and Archard's Laws.

KEYWORDS: modal interaction, spectral analysis, blade-casing contact, blade vibration, wear.

1 INTRODUCTION

Lot of work has been devoted to highlighting the physical phenomena associated with contact and prioritizing their respective influence on possible unstable behavior exhibited in some specific cases by rotating machines. However, the influence of certain phenomena such as wear still require further study. The bibliographical study conducted in [1] has allowed identifying the predominant phenomena during rotor-stator / blade-casing contact. The system's dynamic behavior is determined to be of a nonlinear type, with these non-linearities being introduced by means of phenomena like friction, wear and heating.

Torkhani [2] has highlighted chaotic system behavior in the presence of friction, which becomes "increasingly complex" upon reaching certain coefficient of friction values. The experimental and numerical studies examined in [3, 4] reveal the significant influence of wear and heating phenomena on the dynamic behavior during contact. As a general rule, these two phenomena are handled separately in the simulations. Nonetheless, we have been able to observe the importance of coupling dynamics, thermal expansion and wear, to yield a better understanding of the corresponding interaction phenomena. The modeling of wear has been addressed in the literature according to various approaches. Strömberg [5] and Salles [6] modeled wear using Archard's Law, while Williams [7] and Batailly [4] proposed a plastic behavior law for the abradable coating. Within the scope of this paper, we will be using an Archard Law formulation [8] given its effective representation of the wearing problem, while remaining rather simple to integrate into the simulations.

During contact, the processes of friction and wear influence the dynamic behavior of structures, thus making it necessary to establish the mathematical formulation of an elastodynamic contact problem with friction and wear, for subsequent application to a case of rotor-stator / blade-casing contact. Figure 1 illustrates the entire array of phenomena to be taken into account in this work when setting up the equation.

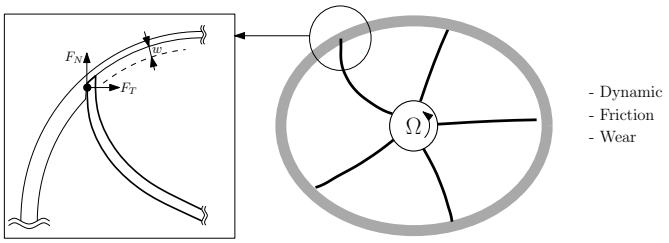

Figure 1. Physical phenomena encountered during blade-casing contact

2 DYNAMICAL MODEL

In this paper, we have implemented a finite element model of a bladed wheel placed in contact with a flexible casing [9]. This bladed wheel model contains four blades modeled by two Euler-Bernoulli beams per blade with six degrees of freedom per node (three displacements and three rotations). The disc is also modeled by Euler-Bernoulli beams that couple the blade to one another, with two degrees of freedom per node: radial displacement and rotation along the axis of rotation. The link with the rotor axis will be set by means of radial tension-compression springs. Moreover, stiffeners have been introduced to connect the blades so as to control tune the modal organization of the bladed wheel.

The casing is modeled by a continuous elastic ring [10] containing two degrees of freedom at every point, i.e. radial displacement $u_s(\theta, t)$ and tangential displacement $w_s(\theta, t)$. The points will be identified by θ, which corresponds to the angular position with respect to the stationary reference.

*Address all correspondence to this author.

Ring displacements will be expressed through use of Ritz functions, in accordance with the procedure described by Love [11]:

$$w_s(\theta,t) = \sum_{n_d=1}^{k_{tot}} A_{n_d}(t)\cos(n_d\theta) + B_{n_d}(t)\sin(n_d\theta) \quad (1)$$

where k_{tot} is the number of nodal diameters (or modes) taken into consideration. The ring is assumed to be inextensible, which implies that radial displacement is correlated with tangential displacement [12]:

$$u_s(\theta,t) = \frac{\delta w_s(\theta,t)}{\delta\theta} \quad (2)$$

The ring thus features $2\,k_{tot}$ degrees of freedom.

The mass and stiffness matrices of the ring are derived by applying the Lagrange equations. For the bladed wheel, the mass and stiffness matrices will be obtained through a conventional finite element formulation. In this manner, resolving the contact problem, with the inclusion of both the friction and wear phenomena, consists of solving the set of bladed wheel - casing system motion equations:

$$\mathbf{M\ddot{u}} + \mathbf{D\dot{u}} + \mathbf{Ku} + \mathbf{F_c} = \mathbf{F_{ext}} \quad (3)$$

where $\mathbf{u}$ is the displacement field, $\mathbf{M}$ the mass matrix, $\mathbf{K}$ the stiffness matrix, $\mathbf{D}$ the structural damping matrix, $\mathbf{F_{ext}}$ the external force vector and $\mathbf{F_c}$ the contact force vector will be obtained through the Lagrange multipliers method.

3 TIME STEP INTEGRATION OF THE CONTACT PROBLEM

An explicit time step finite difference method is used to solve the equations above (9). The stability of an explicit scheme is provided for a time increment Δt less than the critical time increment Δt_{stab}. Following a convergence study, the time increment was set at a value close to a small fraction of the smallest characteristic period of the structures.

The (nonlinear) contact problem is solved by a succession of prediction steps, yet without taking into account the contact forces, followed by corrections in cases where contact has been detected. These steps can be detailed as follows [12, 13].

3.1 Prediction step

The displacements $\mathbf{u}_{n+1}$ are predicted [1], yet without taking into account contact forces and based on known values at previous times n and $n-1$:

$$\mathbf{u}_{n+1,p} = \left[\frac{\mathbf{M}}{\Delta t^2} + \frac{\mathbf{D}}{2\Delta t}\right]^{-1} \left(\mathbf{F_{ext}}_n + \left(2\frac{\mathbf{M}}{\Delta t^2} - \mathbf{K}\right)\mathbf{u}_n + \left(2\frac{\mathbf{M}}{\Delta t^2} - \mathbf{K}\right)\mathbf{u}_n + \left(\frac{\mathbf{D}}{2\Delta t} - \frac{\mathbf{M}}{\Delta t^2}\right)\mathbf{u}_{n-1}\right) \quad (4)$$

The initial distance between the two structures g must be updated using the predicted values, in order to verify Signorini's conditions relative to the unilateral contact.

[1] The index p will be used to declare the prediction step.

Wear is taken into account by applying a law similar to Archard's Law [8] and then following the method described by Salles [14]. To proceed, let's introduce the distance function $g\left(\mathbf{u}_N^M, \mathbf{w}^M\right)$, which is dependent on normal displacement variables as well as wearing depth.

$$g\left(\mathbf{u}_N^M, \mathbf{w}^M\right) = \mathbf{u}_N^M - \mathbf{w}^M - \mathbf{g}^M \quad (5)$$

where $\mathbf{u}_N^M$, $\mathbf{w}^M$ and $\mathbf{g}^M$ are respectively the normal displacement, wearing depth and initial gap calculated on a set of contact points $\mathbf{x}^M$.

The contact takes place if $g\left(\mathbf{u}_N^M, \mathbf{w}^M\right)$ fails to satisfy the non-penetration condition predicted during step $n+1$:

$$g\left(\mathbf{u}_N^M, \mathbf{w}^M\right)_{n+1,p} \leq 0 \quad (6)$$

The normal displacement vector in step $n+1$ is deduced from Equation (4). On the other hand, the wearing depth vector will be calculated after the correction step (see Eq. (14)) since the normal contact force needs to be known first; this force will be determined during the next step. The wearing depth vector value will thus be introduced during step n in order to verify the non-penetration conditions (7).

$$\mathbf{u}_{Nn+1,p}^M - \mathbf{w}_n^M - \mathbf{g}^M \leq 0 \quad (7)$$

3.2 Correction step

If according to the predicted values the rotor penetrates into the stator, the degrees of freedom would need to be corrected to ensure verification of the non-penetration condition (8) as well as the force equilibrium condition (9):

$$g\left(\mathbf{u}_N^M, \mathbf{w}^M\right)_{n+1} = g\left(\mathbf{u}_N^M, \mathbf{w}^M\right)_{n+1,p} + {}^t\mathbf{C_N}_{n+1,p} \cdot \delta\mathbf{u}_{n+1}^M \quad (8)$$

$$\left(\frac{\mathbf{M}}{\Delta t^2} + \frac{\mathbf{D}}{2\Delta t}\right)\left(\mathbf{u}_{n+1} + \delta\mathbf{u}_{n+1}^M\right) = \mathbf{F_{ext}}_n + \mathbf{F_c}_{n+1} + \left(2\frac{\mathbf{M}}{\Delta t^2} - \mathbf{K}\right)\mathbf{u}_n + \left(\frac{\mathbf{D}}{2\Delta t} - \frac{\mathbf{M}}{\Delta t^2}\right)\mathbf{u}_{n-1} \quad (9)$$

where $\delta\mathbf{u}_{n+1}^M$ are the corrections to consider for the purpose of validating both conditions, and $\mathbf{C_N}$ is the linearized vector yielding the normal force direction along with the displacement corrections direction. $\mathbf{F_c}_{n+1}$ is the vector of forces due to the contact and may be expressed according to the Lagrange multipliers method by:

$$\mathbf{F_c} = \mathbf{F_c}_N + \mathbf{F_c}_T = -\left[\mathbf{C_N} + \mathbf{C_T}\right]\lambda_N = -\mathbf{C_{NT}}\lambda_N \quad (10)$$

where $\mathbf{C_T}$ is the linearized vector yielding the friction force direction and λ_N is the Lagrange multiplier. $\mathbf{C_T}$ was derived by using Coulomb's Law during its sliding phase (permanent sliding), thus meaning that it depends on the coefficient of friction μ.

The compatibility conditions of displacements and equilibrium forces that need to be verified by the corrected degrees of freedom are written, in the case of several contacts (i.e. a contact occurs at the different points belonging to the subset $\mathbf{x}^M$), just like equations (8) and (9), but in vector form:

$$\mathbf{g}_{n+1} \approx \mathbf{g}_{n+1,p} + {}^t\mathbf{C_N}_{n+1,p} \cdot \delta\mathbf{u}_{n+1}^M = 0 \quad (11)$$

$$\left(\frac{\mathbf{M}}{\Delta t^2}+\frac{\mathbf{D}}{2\Delta t}\right)\delta\mathbf{u}^M_{n+1}=-\mathbf{C_{NT}}_{n+1,p}\lambda_{\mathbf{N}n+1} \tag{12}$$

The system of equations resulting in $\lambda_{\mathbf{N}n+1}$ and $\delta\mathbf{u}^M_{n+1}$ still needs to be solved.

$$\begin{cases} \lambda_{\mathbf{N}n+1}=\left[\mathbf{C_N}^T_{n+1,p}\left(\frac{\mathbf{M}}{\Delta t^2}+\frac{\mathbf{D}}{2\Delta t}\right)^{-1}\mathbf{C_{NT}}_{n+1,p}\right]^{-1}\mathbf{g}_{n+1,p} \\ \delta\mathbf{u}^M_{n+1}=-\left(\frac{\mathbf{M}}{\Delta t^2}+\frac{\mathbf{D}}{2\Delta t}\right)^{-1}\mathbf{C_{NT}}_{n+1,p}\lambda_{\mathbf{N}n+1} \end{cases} \tag{13}$$

At each time interval, the expressions for $\mathbf{g}_{n+1,p}$, $\mathbf{C_N}_{n+1,p}$ and $\mathbf{C_{NT}}_{n+1,p}$ must be calculated on the basis of predicted values and with the accuracy required to ensure convergence.

Once the contact force calculation has been executed, we are in a position to calculate the wearing depth vector obtained by:

$$\mathbf{w}^M_{n+1}=\frac{\Delta t}{2}\left(k_w|P_{Nn+1}|\left\|\dot{\mathbf{u}}^M_{Tn+1}\right\|+\dot{\mathbf{w}}^M_n\right)+\mathbf{w}^M_n \tag{14}$$

where k_w is the coefficient of wear intensity appearing in Archard's Law and P_N the normal contact pressure.

4 SIMULATION RESULTS

The objective of this work program is to test the influence of both friction and wear on the dynamic behavior in a situation of blade-casing contact. To achieve this objective, the values of the coefficient of friction and Archard Law's coefficient of wear intensity will be varied.

Contact is initiated by exciting a mode with one diameter on the stator with a stationary wave whose amplitude is sufficient to cover the clearance between the two structures. The simulations presented were run at the constant rotational speed corresponding to case A in Figure 2, where a modal interaction is expected between the backward mode of the casing and the counter-rotation mode of the bladed wheel with one diameter [1].

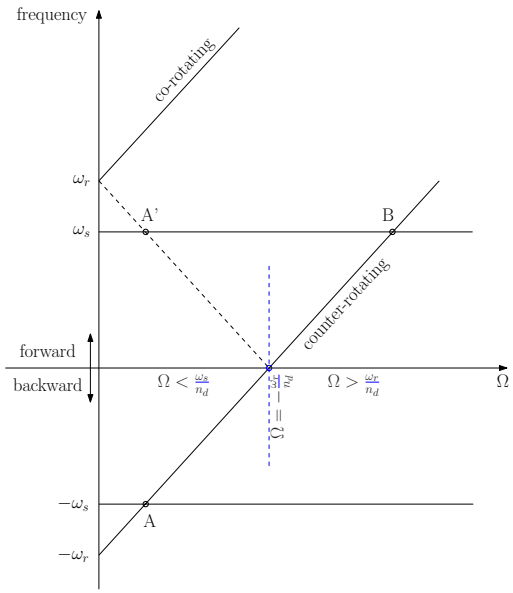

Figure 2. Campbell diagram in stationary frame

The frequency content of simulations will be analyzed with two spectral analysis tools. The Short-Time Fourier Transform - or STFT - will then serve to visualize spectrum changes vs. time [15]. The two-dimensional Discrete Fourier Transform - 2D DFT - will determine the spatial decomposition into nodal diameters for each spectrum frequency. An analysis of the complete spatial spectrum reveals the modal decomposition in forward (FW) participation and backward (BW) participation for a given diameter [16]. The frequency analysis will be carried out over the range of initial bending modes $[0-4000Hz]$.

4.1 *Reference simulation*

Different simulated cases will be compared to a reference configuration, whose values are: $\mu=0.1$ and $k_w=0$. The time-frequency analysis (see Fig. 3) was conducted in using both the tangential displacement of the blade tip and the radial displacement of the casing. On these same figures, indications are provided of the eigenfrequencies of the respective free structures, the rotational speed harmonics present within the spectrum and the excitation frequency with associated main rays coming from modulations by the rotational speed. Figure 3a shows the stator response to the external excitation introduced to initiate contact. As it may be observed, the excitation frequency F_{exct} does indeed excite the mode at one diameter from the structure ω^1_s, since $F_{exct}=\omega^1_s$. It can be checked that the response has actually one nodal diameter in Figure 4. Note that the frequency F_{exct} of the main component in the stator response known to be a one nodal diameter would be seen at $F_{exct}+1\,\Omega$ where a dominant component actually takes place. This could be interpreted as the system transmitting vibration frequencies from one structure to the other by means of contact forces.
Moreover, the presence of the fourth harmonic of rotational speed ($4\,\Omega$) can be seen as well as the excitation frequency modulation by four times the rotational speed $F_{exct}+4\,\Omega$. Frequency components appearing within the signal spectrum will be called *side-bands* [17] in the remainder of this paper. This will related to an amplitude modulation at frequency Ω of the excitation frequency F_{exct}.

The bladed wheel spectrum (Fig. 3b) is characterized by a component closed to the rotor ω^1_r (a rotor mode with one diameter), which coincides with the mode with one diameter from the stator, as observed in the rotating reference frame $\omega^1_r=\omega^1_s+1\,\Omega=F_{exct}+1\,\Omega$. The second harmonic ($2\,\Omega$), fourth harmonic ($4\,\Omega$), sixth harmonic ($6\,\Omega$) and twelfth harmonic ($12\,\Omega$) of rotational speed are also found, along with the odd *side-bands* from $F_{exct}\pm1\,\Omega$ to $F_{exct}\pm3\,\Omega$. The second harmonic of excitation frequencies $2\,F_{exct}$ is also present, as are its even side-bands at $2\,F_{exct}\pm2\,\Omega$, $2\,F_{exct}-4\,\Omega$ and $2\,F_{exct}-6\,\Omega$.

It can be demonstrated that these *side-bands* are nonlinear combinations of the excitation frequency and the rotational speed harmonics (see §5). The frequencies of these *side-bands* track the relation:

$$f^k_{SB}=F_{exct}+k\,\Omega \qquad \text{for} \quad k\in\mathbb{Z} \tag{15}$$

where f^k_{SB} is the *side-band* frequency of order k and F_{exct} is the excitation frequency of the casing.

The two-dimensional Discrete Fourier Transform or frequency-nodal diameter diagram shown in Figure 4 indicates that a stationary wave with one diameter at $F_{exct}=1417Hz$ is indeed present, while the bladed wheel response is dominated by a backward wave at one diameter to

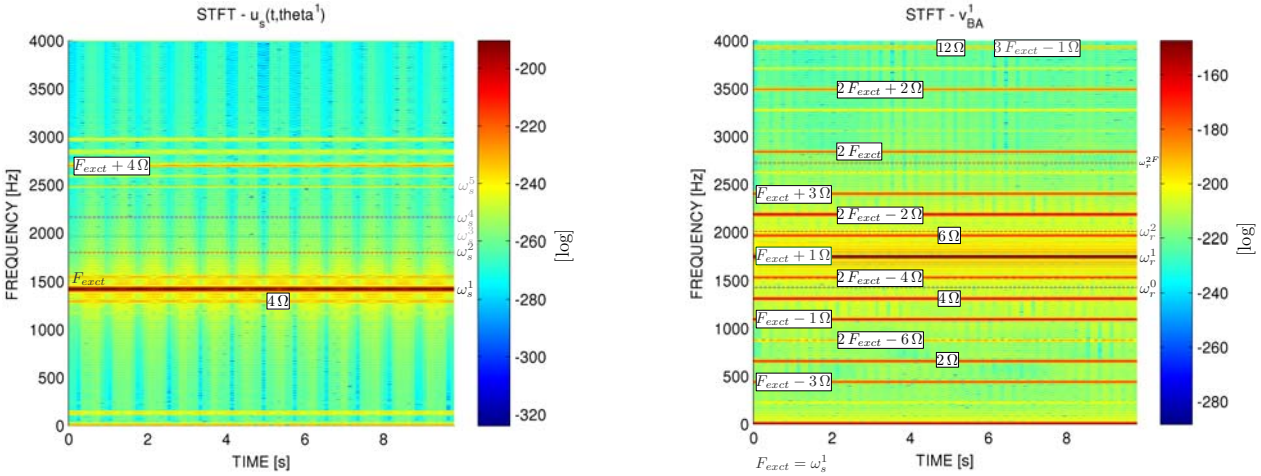

(a) Casing (b) Bladed wheel

Figure 3. STFT of the first family modes of both structures, with $\mu = 0.1$

$F_{exct} + 1\,\Omega = \omega_r^1$ in accordance to case A in the Campbell diagram (Fig. 2).

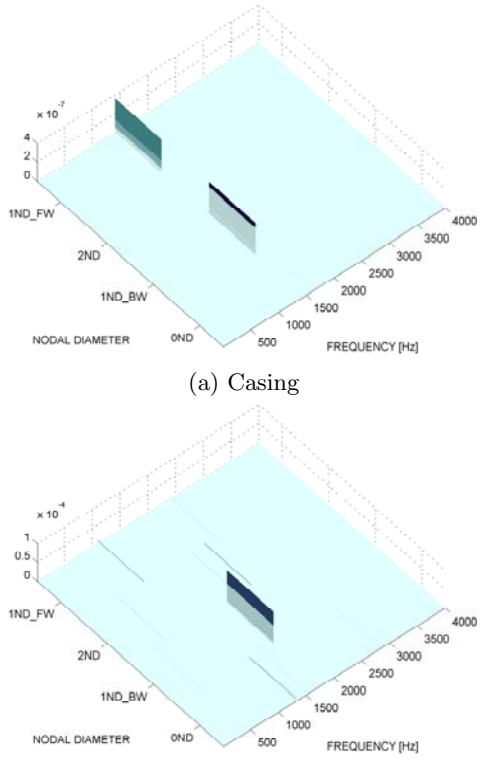

(a) Casing

(b) Bladed wheel

Figure 4. 2D DFT diagram of the first-family modes of both structures with $\mu = 0.1$

4.2 *Influence of friction*

Firstly, attention will be solely paid to the influence of the coefficient of friction (calculations without wear) based on the following values: $\mu = 0; 0.05; 0.1; 0.15; 0.2$. Figure 5 shows the time response of the tangential displacement of a particular blade tip. Two distinct types of behavior can be observed depending on the chosen value of μ. For $\mu = 0; 0.05; 0.1$, the blade bends and vibrates around its static equilibrium position with intermittent contact. For $\mu = 0.15; 0.2$, after a short transient response, the blades exhibit a quasi-static behavior. The vibration response of the bladed wheel thus depends on the coefficient of friction and displays a maximum at an intermediate μ value. For higher μ values, the blades are in permanent contact with the stator and exhibit a static deformation with a zero diameter spatial shape. On the stator side, the frequency response is dominated by a $4\,\Omega$ component with a four-diameter deformed shape that propagates in the forward direction at propagation speed Ω. This could be interpreted has a rotating deformed shaped imposed to the flexible stator by the four blades. This indeed results in a vibration at $4\,\Omega$ frequency.

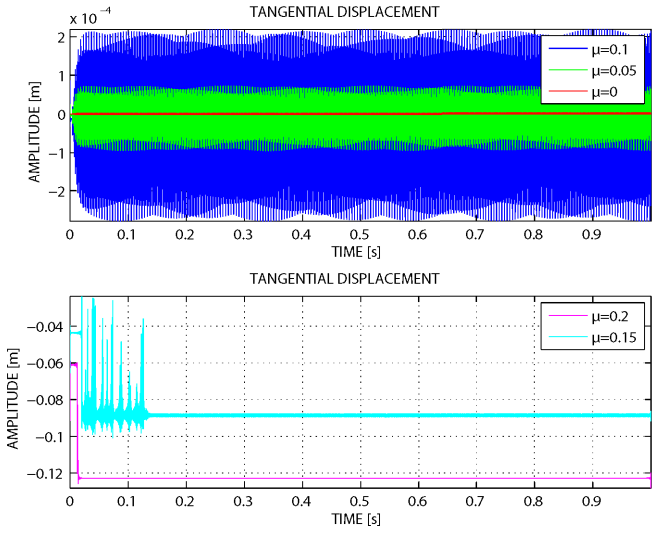

Figure 5. Influence of friction

The spectrograms shown in Figure 6 for $\mu = 0$ and $\mu = 0.05$ will be compared to the spectrogram of Figure 3b. Aside from the amplitude difference, as highlighted by examining the temporal responses (Fig. 5), it can be observed that for a zero coefficient of friction (see Fig. 6a), the second harmonic of the excitation frequency and its

side-bands are absent from the spectrum, as are the second ($2\,\Omega$) and fourth ($2\,\Omega$) rotating frequency harmonics. On the other hand, with a coefficient of friction equal to $\mu = 0.05$, all of the frequency components present in the reference simulation are available, yet at lower levels.

4.3 *Influence of wear*

Starting with the reference configuration at $\mu = 0.1$, the value of Archard Law's coefficient of wear intensity will be varied. The following values will be used herein: $k_w^* = 0.1; 1; 10$. In order to facilitate the interpretation, these values were normalized. The introduction of wear results in an attenuation of the vibrations given that abradable material is removed by the wear process; hence, the clearance between the casing and blade tips increases. The wear maps shown in Figure 7 indicate that contact occurs in two diametrically opposite places. This map corresponds to a two-lobe wear profile. A comparison of these maps reveals that for higher values of Archard Law's coefficient, the wear lobes will be generated more quickly.

In Figure 8, the temporal response of the tangential displacement of a blade has been plotted for the three tested coefficients. It can be noticed that as the wearing coefficient rises, the response decay is faster.

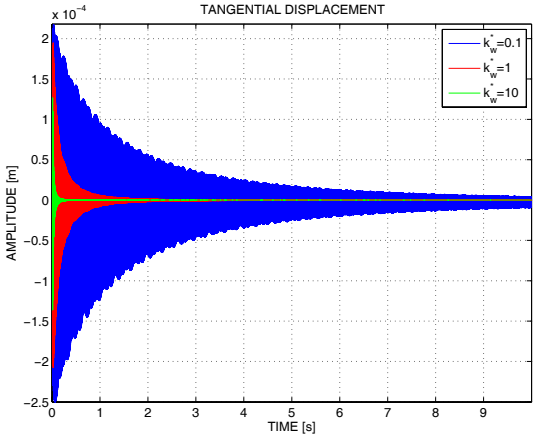

Figure 8. Influence of wear

As opposed to the influence of the coefficient of friction, the variation in Archard's coefficient of wear intensity exerts no influence on the spectrum content. In other words, all simulations run with wear expose the same *side-bands* and rotational speed harmonics with respect to the reference simulation. Nonetheless, as the coefficient of wear increases, its terms will gradually drop their level over time. As such, it is observed that all *side-bands* and rotational speed harmonics disappeared after two seconds for the simulation at $k_w^* = 10$, although they remain present after ten seconds with the simulation at $k_w^* = 0.1$.

5 RESULTS INTERPRETATION

During simulation runs, we mainly encountered rotational speed harmonics and *side-bands*. In the spectrograms under analysis, *side-bands* are actually observed at a distance of multiple Ω relative to an excited frequency. The presence of the rotational speed harmonics is obviously expected as part of a rotating system. In contrast, such is not the case for the *side-bands*; consequently, this section of the paper is intended to offer a qualitative explanation of the spectral content found numerically.

To pursue this objective, let's begin by assigning a definition of *side-bands*, before introducing an analytical model that will lead to discovering the various terms encountered in the simulations. Let's also note that the qualitative comparison with the numerical part will take place between the calculated force and the measured displacements.

In the simplified approach below, structural displacements are forced and the focus lies on the resultant contact force spectrum.

5.1 *Side-bands definition*

Side-bands appearing within a signal spectrum are the outcome of an amplitude modulation of a so-called carrier frequency by a so-called modulating frequency. The spectrum will then be characterized by two side bands offset by the modulating frequency and centered around the carrier frequency.

If we consider ω_0 as the carrier frequency and Ω as the modulating frequency, the modulated signal will thus be given in the temporal domain by the expression (16) :

$$s(t) = cos\,(\omega_0\,t)\;cos\,(\Omega\,t) \tag{16}$$

The shape of the signal resulting from a current multiplication of beats within the temporal domain. In the spectral domain, this signal will be:

$$S\,(\omega) = \delta_{\omega_0-\Omega} + \delta_{\omega_0+\Omega} \tag{17}$$

The spectrum therefore contains two bands $\omega_0 - \Omega$ and $\omega_0 + \Omega$, which have been called *side-bands* herein.

5.2 *Problem set-up*

Note that the definition above can explain a limited number of observed *side-bands*. To better understand the origin of *side-bands* encountered during simulations, we will be introducing an analytical model of the contact force law between a blade on the bladed wheel and its casing (see Fig. 10), which will be tested by entering into a reference displacement.

The displacements of both structures will be modeled by harmonic functions, while the contact force will obey to a law that contains a linear part and a nonlinear part. For purposes of this paper, let's take a closer look at the frequency content of the contact force with a second order polynomial non-linear function.

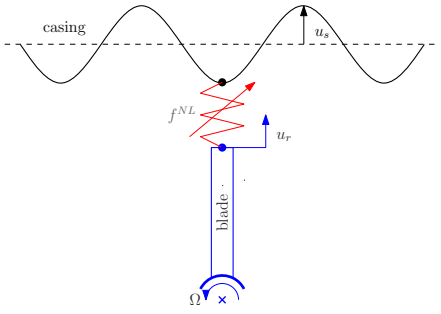

Figure 10. Simplified model of a blade in contact with the casing

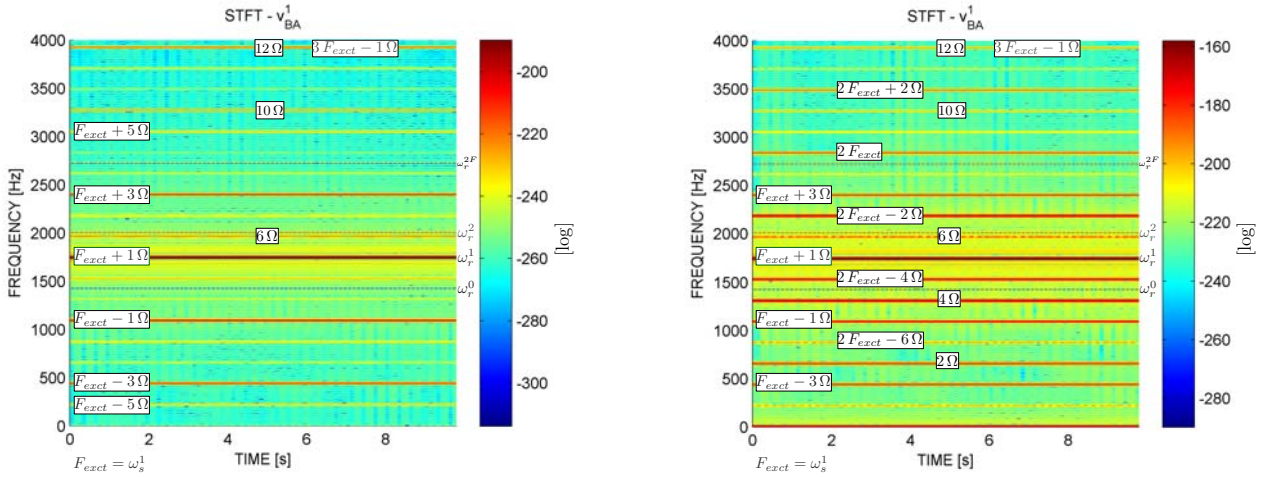

(a) $\mu = 0$ (b) $\mu = 0.05$

Figure 6. Influence of friction on the blade response spectrogram (rotating frame)

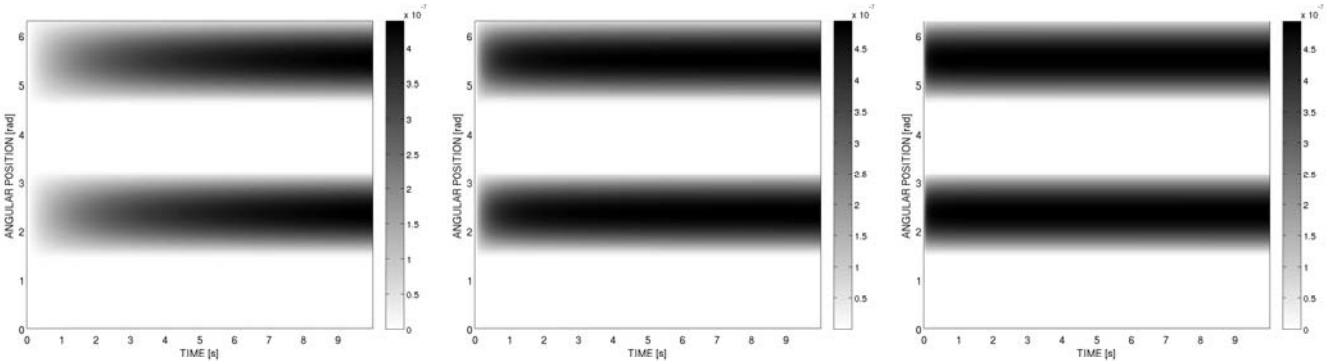

(a) $k^*_w = 0.1$ (b) $k^*_w = 1$ (c) $k^*_w = 10$

Figure 7. Time history of wear patterns

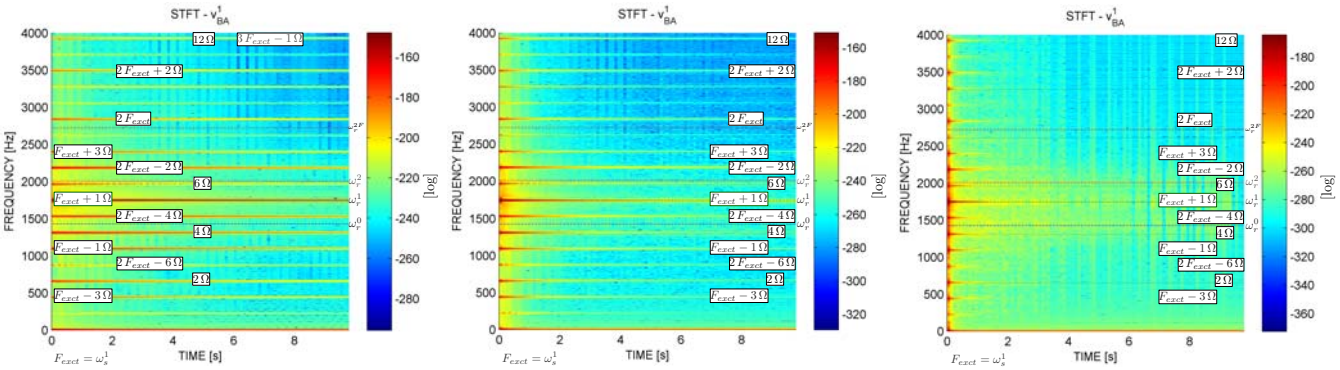

(a) $k^*_w = 0.1$ (b) $k^*_w = 1$ (c) $k^*_w = 10$

Figure 9. Influence of wear on the blade response spectrogram

The (purely radial) displacement of a blade will be defined within the rotating reference frame by:

$$u_r\left(t,\theta_R\right) = U_r \cdot cos\left(\omega_r\, t\right) \cdot cos\left(n_d^r\, \theta_R\right) \tag{18}$$

with U_r being the blade displacement amplitude, ω_r the eigenfrequency of the bladed wheel, n_d^r the number of diameters in the bladed wheel wave and θ_R the angular position of the blade within the rotating reference frame. According to Equation (18), the field u_r is a stationary wave. In a more general case, u_r will be of the following form:

$$u_r\left(t,\theta_R\right) = U_r^{bw} \cdot cos\left(\omega_r\, t + n_d^r\, \theta_R\right) + U_r^{fw} \cdot cos\left(\omega_r\, t - n_d^r\, \theta_R\right) \tag{19}$$

where U_r^{bw} and U_r^{fw} are respectively the counter-rotating and co-rotating component amplitudes of the displacement wave for a blade on the bladed wheel. Although, the form given in Equation (18) is sufficient for the demonstration.

Let's note that the expressions in (18) and (19) are equivalent with respect to the reference θ_R whenever $U_r^{fw} = U_r^{bw} = U_r/2$.

The casing displacement will also be defined by a stationary wave within the stationary reference frame:

$$u_s\left(t,\theta_S\right) = U_s \cdot cos\left(\omega_s\, t\right) \cdot cos\left(n_d^s\, \theta_S\right) \tag{20}$$

with U_s the casing displacement amplitude, ω_s the eigenfrequency of the casing, n_d^s the number of diameters of the casing wave and θ_S the angular position of the blade relative to the stationary reference frame.

The displacements of both structures will be expressed in the rotating reference frame prior to being injected into the force function. To proceed, we will use Equation (21) to transition from the stationary reference frame to the rotating one:

$$\theta_S = \theta_R + \Omega\, t \tag{21}$$

Within the rotating frame, the casing displacement then becomes:

$$u_s\left(t,\theta_R\right) = U_s \cdot cos\left(\omega_s\, t\right) \cdot cos\left(n_d^s\, \theta_R + n_d^s\, \Omega\, t\right) \tag{22}$$

Let's note that in decomposing the second term into *cos*, only the stationary stator wave is actually exposed. Given the rotating reference frame, this decomposition step gives rise to two waves traveling in opposite directions.

The contact force between the two structures will be defined by Equation (23), which comprises a linear part and a second-order nonlinear part. We have actually selected a regular non-linearity that is both even and simple to process analytically to ensure being representative of the contact law in some point.

$$f\left(t,\theta_R\right) = \alpha_1\left(u_r - u_s\right) + \alpha_2\left(u_r - u_s\right)^2 \tag{23}$$

where α_1 and α_2 are contact stiffness coefficients.

By inserting (18) and (22) into (23) and in adopting the special case in which $\alpha_1 = \alpha_2 = \alpha$ out of simplification, the contact force expression will assume the following form:

$$\begin{aligned} f\left(t,\theta_R\right) \;=\; \alpha \Bigg[& \frac{U_r^2}{4} + \frac{U_s^2}{4} \\ & + \frac{U_r}{2} cos\left(\omega_r\, t \pm n_d^r\, \theta_R\right) \\ & - \frac{U_s}{2} cos\left(\omega_s\, t \pm \left(n_d^s\, \theta_R + n_d^s\, \Omega\, t\right)\right) \\ & + \frac{U_r^2}{4}\left(cos\left(2\,\omega_r\, t\right) + cos\left(2\, n_d^r\, \theta_R\right)\right) \\ & + \frac{U_s^2}{4}\left(cos\left(2\,\omega_s\, t\right) + cos\left(2\left(n_d^r\, \theta_R + n_d^s\, \Omega\, t\right)\right)\right) \\ & + \frac{U_r^2}{8} cos\left(2\,\omega_r\, t \pm 2\, n_d^r\, \theta_R\right) \\ & + \frac{U_s^2}{8} cos\left(2\,\omega_s\, t \pm 2\left(n_d^s\, \theta_R + n_d^s\, \Omega\, t\right)\right) \\ & - \frac{U_r\, U_s}{4} cos\left(\omega_r\, t \pm n_d^r\, \theta_r \pm \omega_s\, t \pm \left(n_d^s\, \theta_R + n_d^s\, \Omega\, t\right)\right) \Bigg] \end{aligned} \tag{24}$$

The previous equation and subsequent expressions make use of a contracted notation for the multiplication of two cosines; instead of writing $cos(a) \cdot cos(b) = \frac{1}{2}\left[cos(a+b) + cos(a-b)\right]$, we will write $cos(a) \cdot cos(b) = \frac{1}{2}\, cos(a \pm b)$. This notation may also be generalized. The final row of (24) contains eight terms according to this notation.

The expression in (24) displays in order: nonlinear static terms ($\omega = 0$), the linear terms, and some other nonlinear terms. The frequencies and corresponding nodal diameters presents in the system are listed in Tables 1 and 2. Table 1 provides the nodal diameters and frequencies obtained when only considering a linear contact, whereas Table 2 shows the nodal diameters and frequencies obtained when solely accounting for a second-degree nonlinear force. The spectral content of the contact force will be composed of frequencies stemming from both the linear and nonlinear contact forces. Terms appearing in the analytical force expression are in good accordance with the spectrum of the numerically simulated response. In particular, one could notice the presence of several even terms associated to the contact nonlinearity.

Linear force law	$f^L = \alpha\left(u_r - u_s\right)$	
Frequencies $[rad/s]$	ω_r	$\omega_s \pm n_d^s\, \Omega$
Nodal diameters	n_d^r	n_d^s

Table 1. Frequencies and nodal diameters obtained with a linear contact force interaction in the rotating frame

The purely linear case enables identifying the angular eigenfrequencies of both structures expressed in the rotating reference frame. From a spatial perspective, the force field is a superposition of the two fields with n_d^s and n_d^r nodal diameters (second and third rows in (24)).

The purely nonlinear case exbibits the presence of static terms (i.e. zero frequency), the second harmonic of the angular eigenfrequencies of structures expressed or not in the rotating frame ($2\,\omega_r$, $2\,\omega_s$, $2\ (\omega_s \pm n_d^s\, \Omega)$), the $2\, n_d^s$ rotating speed harmonic and lastly the combination of eigenfrequencies of structures within the rotating frame (this term was not numerically observed). The presence of the second harmonic is correlated with the chosen non-linearity, which in this case is of the second order.

From this analysis, it seems that the presence of the rotational speed harmonics and *side-bands* will be guided

2^{nd}-order nonlinear force	$f^{NL} = \alpha\,(u_r - u_s)^2$						
Frequencies $[rad/s]$	0		$2\,\omega_r$	$2\,\omega_s$	$2\,n_d^s\,\Omega$	$2\,(\omega_s \pm n_d^s\,\Omega)$	$\omega_r \pm \omega_s \pm n_d^s\,\Omega$
Nodal diameters	0	$2\,n_d^r$	$2\,n_d^r$		$2\,n_d^s$		$\pm n_d^r \pm n_d^s$

Table 2. Frequencies and nodal diameters obtained with a 2^{nd}-order nonlinear contact force interaction with an harmonic input

by the contact law, and more specifically by the degree of non-linearity. Consequently, we are able to improve the contact law approximation for any order N by applying Equation (25):

$$f^N = \sum_{n=0}^{N} \alpha_n\,(u_r - u_s)^n = \sum_{n=0}^{N} \alpha_n \left[\sum_{p=0}^{n} C_n^p\,u_r^p\,(-u_s)^{n-p}\right] \tag{25}$$

where f^N is the contact force formulated with a degree of non-linearity extending all the way to order N.

We can see that a mean to increasing the number of *side-bands* and rotational speed harmonics would be to raise the value of N in Equation (25).

The same would apply in the frequency domain, as spatially the number of harmonics will depend on the selected degree of non-linearity.

One could easily understand that if the polynomial degree approximating the contact law were to be raised, then the contact force spectrum would become richer. The Figure 11 shows the spectrum of a contact law that follows exactly Signorini's unilateral law with a single harmonic input. It is observed that only the fundamental (input frequency) and even harmonics are noteworthy and therefore characterize this contact law. In the case of the rotating blade with Signorini law the spectrum will therefore contains for instance every terms in the form $2\,p\,n_d^s\,\Omega$ with $p = 0, 1, 2, ...$ (see Table 2).

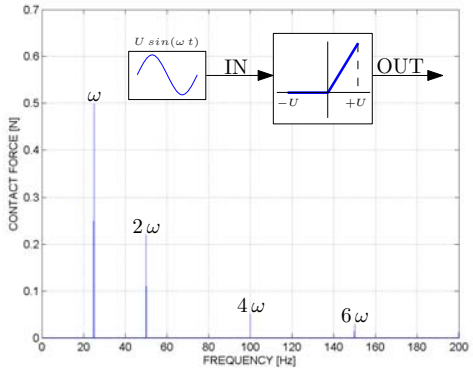

Figure 11. Output amplitude spectrum of the Signorini's unilateral contact law with an harmonic input

6 CONCLUSION

A numerical model allowing for the incorporation of blade-casing friction and wear contact has been built herein. The integration method has used the Lagrange multipliers method along with an explicit time marching scheme. A sensitivity study with respect to both Coulomb Law and Archard Law parameters has been conducted in conjunction with a campaign of numerical simulations. A one dimensional spectral analysis on the time and a two dimensional analysis in space domain has been used to characterize the frequency content and type of waves.

Depending on the coefficient of friction value, we have observed two distinct types of behavior from the perspective of the bladed wheel, one dynamic the other quasi-static. In the case with dynamic behavior, two wearing lobes were obtained on the stator per each revolution. These findings were derived with synchronous vibrations at one diameter on both stator and rotor. Put otherwise, all blades touch twice per revolution and always in the same stator zone. The introduction of wear into the system has made it possible to attenuate vibration amplitudes.

The spectral analysis has demonstrated the presence of many *side-bands* and harmonics as a function of the level of vibration; as shown with a simple analytical model, these features can be explained by the contact non-linearity between rotor and stator.

AKNOWLEDGMENT

This work was partially funded by the French National Research Agency (ANR), within the framework of its COSINUS Technological Research program (IRINA project, ref. ANR 09 COSI 008 01 IRINA).

References

[1] Jacquet-Richardet, G., Torkhani, M., Cartraud, P., Thouverez, F., Nouri Baranger, T., Herran, M., Gibert, C., Baguet, S., Almeida, P., and Peletan, L. "Rotor to stator contacts in turbomachines. review and application". Mechanical Systems and Signal Processing. 1, 3

[2] Torkhani, M., May, L., and Voinis, P., 2012. "Light, medium and heavy partial rubs during speed transients of rotating machines: Numerical simulation and experimental observation". Mechanical Systems and Signal Processing, **29**, pp. 45–66. 1

[3] Millecamps, A., Brunel, J.-F., Dufrenoy, P., Garcin, F., and Nucci, M., 2009. "Influence of thermal effects during blade-casing contact experiments". ASME Conference Proceedings, **2009**(48982), Jan., pp. 855–862. 1

[4] Batailly, A., Legrand, M., Millecamps, A., and Garcin, F., 2012. "Numerical-experimental comparison in the simulation of Rotor/Stator interaction through blade-Tip/Abradable coating contact". Journal of Engineering for Gas Turbines and Power, **134**(8), pp. 082504–082504. 1

[5] Strömberg, N., 1999. "Finite element treatment of two-dimensional thermoelastic wear problems". Computer Methods in Applied Mechanics and Engineering, **177**(3-4), July, pp. 441–455. 1

[6] Salles, L., Blanc, L., Thouverez, F., Gouskov, A., and Jean, P., 2012. "Dual time stepping algorithms with the high order harmonic balance method for contact interfaces with fretting-wear". Journal of Engineering for Gas Turbines and Power, **134**(3). 1

[7] Williams, R., 2011. "Simulation of blade casing interaction phenomena in gas turbines resulting from heavy tip rubs using an implicit time marching method". In Proceedings of the ASME Turbo Expo, Vol. 6, pp. 1007–1016. 1

[8] Archard, J. F., 1953. "Contact and rubbing of flat surfaces". Journal of Applied Physics, **24**. 1, 2

[9] Legrand, M., 2005. "Modèles de prédiction de l'interaction rotor/stator dans un moteur d'avion". PhD thesis, Ecole Centrale de Nantes, Nantes, France. 1

[10] Lesaffre, N., Sinou, J.-J., and Thouverez, F., 2007. "Contact analysis of a flexible bladed-rotor". European Journal of Mechanics - A/Solids, **26**(3), pp. 541–557. 1

[11] Love, A. E. H., 1906. A treatise on the mathematical theory of elasticity. Cambridge : University Press. 2

[12] Lesaffre, N., 2007. "Stabilité et analyse non-linéaire du contact rotor-stator". PhD thesis, Stabilité et analyse non-linéaire du contact rotor-Stator, Lyon, France. 2

[13] Legrand, M., Pierre, C., Cartraud, P., and Lombard, J.-P., 2009. "Two-dimensional modeling of an aircraft engine structural bladed disk-casing modal interaction". Journal of Sound and Vibration, **319**(1-2), Jan., pp. 366–391. 2

[14] Salles, L., 2010. "Etude de l'usure par fretting sous chargements dynamiques dans les interfaces frottantes : application aux pieds d'aubes de turbomachines". thesis, Ecole centrale de Lyon, Dec. 2

[15] Al-Badour, F., Sunar, M., and Cheded, L., 2011. "Vibration analysis of rotating machinery using time–frequency analysis and wavelet techniques". Mechanical Systems and Signal Processing, **25**(6), Aug., pp. 2083–2101. 3

[16] Almeida, P., Gibert, C., Leblanc, X., Ousty, J.-P., and Thouverez, F., 2012. "Experimental and numerical investigations on a rotating centrifugal compressor". Proceedings of the ASME Turbo Expo, June, pp. 1133–1142. 3

[17] Shmaliy, Y., 2006. Continuous-Time Signals. Springer, Oct. 3